The dynamic response of coseismic liquefaction-induced ruptures associated with the 2019 M_w 5.8 Mirpur, Pakistan, earthquake using HVSR measurements

Muhammad Younis Khan[1], Syed Ali Turab[1], Liaqat Ali[1], Muhammad Tahir Shah[1], S. M. Talha Qadri[2], Khalid Latif[1], Ali Ismet Kanli[3], and Muhammad Gulraiz Akhter[4,5]

https://doi.org/10.1190/tle40080590.1

Redistribution subject to SEG license or copyright; see Terms of Use at http://library.seg.org/page/policies/terms
DOI:10.1190/tle40080590.1

Abstract

The Mirpur area of Pakistan was severely damaged by extensive coseismic liquefaction following an earthquake of M_w 5.8 on 24 September 2019. Villages within 6 km of the epicenter were adversely affected due to extensive coseismic liquefaction-induced surface and shallow subsurface deformations. The earthquake affected all types of buildings and key infrastructure (e.g., the Upper Jhelum Canal and the main Jhelum–Jatlan road). Field observations and associated effects are presented, including horizontal-to-vertical spectral ratio (HVSR) data sets acquired from three sites to evaluate the site response characteristics of the liquefaction-affected soil profiles. As a result, rupture events strongly influenced spectral features (amplitude and frequency) and site-specific 1D shear-wave velocity profiles at sites S1 and S2. The dynamic behavior of HVSRs across ruptures at sites S1 and S2 corresponds to varied levels of seismic amplification, demonstrating the impact of liquefaction-induced ruptures of seismic origin on the site response that have not been reported previously in the literature. The consistent HVSR pattern of well-established high-frequency peaks at site S3 adjacent to partially damaged to completely collapsed buildings of different types further indicates the susceptibility of potential liquefaction hazard. These results agree with the surface liquefaction signatures in the field, revealed by inverted electrical resistivity tomography models in terms of liquified sand plugs, clay lenses and associated fractures, and increasing trends of radon concentration in the soil with decrease in the distance toward ruptures. Additionally, the successful application of HVSR as a cost-effective and speedy tool attests to the potential of the proposed approach in furnishing complementary information for better assessment of liquefaction hazards in the developing world, where financial constraints are a major issue. This can help with seismic hazard analysis and mitigation in the Mirpur area and may have applications in other seismically active regions of the world.

Introduction

Pakistan is considered among the most seismically active zones in the world due to ongoing collision between the Eurasian and Indian plates resulting in the convergence of the latter at a rate of 50 mm/year (Alvarez, 2010). Given the active tectonism, difficult terrain, and climatic factors, northern Pakistan has experienced massive earthquakes, including one of M_w 7.6 that struck the Kashmir region, and thousands of landslides that have had devastating impacts on society and the economy (Shafique and Khan, 2015; Khan et al., 2021). During an earthquake, considerable ground shaking results in an enhanced pore-fluid pressure transforming granular materials from a solid into a liquefied state. This transformation phenomenon, determined by the cyclical seismic shock, is known as liquefaction (Youd, 1977; Jefferies and Been, 2015). It typically occurs in fine and coarse sands, but it also can occur in sandy conglomerates (Takahama et al., 2000; Owen and Moretti, 2011). The minimum earthquake magnitude capable of inducing liquefaction is M_w 5–6 in the near surface (upper 5 m) (Galli, 2000; Owen et al., 2011; Shao et al., 2020). When the increased pore pressure exceeds the overburden pressure, it results in fluidization, which subsequently produces ruptures on the ground, subsidence, lateral spreading, and sand blow features (Youd, 1995). Among other earthquake-related geohazards (tsunamis, landslides, landslide dams, and rockfalls), coseismic liquefaction has gained relatively less attention in spite of causing casualties and extensive damage to houses, roads, lifeline facilities, and other infrastructure by generating ground ruptures that can be tens of meters long (Galli et al., 2012; Orense et al., 2012). The damage to the built environment and/or the population during an earthquake is related to the intensity and duration of ground shaking, which in turn are determined by the earthquake's magnitude and depth, topography, distance from the epicenter, medium of the seismic waves, and site-specific geology. Experiences from past earthquakes in the region (e.g., the 2005 Kashmir earthquake) as well as in other parts of the world have revealed that local soil conditions play an important role in amplifying seismic waves and hence can be considered an important parameter that can exacerbate the level of damage (Borcherdt and Glassmoyer, 1992). Therefore, soil condition assessment is considered a prerequisite in earthquake engineering investigations, and thereby the amplification phenomenon exhibited by surface soil layers often termed as site effects is used in reliable seismic hazard analyses.

[1]University of Peshawar, National Centre of Excellence in Geology, Peshawar, Pakistan. E-mail: myouniskhan@uop.edu.pk; aliturab@uop.edu.pk; liaqat.nceg@uop.edu.pk; tahir_shah@uop.edu.pk; khalidlatif@uop.edu.pk.
[2]University of the Fraser Valley, School of Land Use and Environmental Change, Abbotsford, British Columbia, Canada. E-mail: talhaqadri_uos@hotmail.com.
[3]Istanbul University-Cerrahpasa, Avcilar Campus, Department of Geophysical Engineering, Istanbul, Turkey. E-mail: kanli@istanbul.edu.tr.
[4]China-Pakistan Joint Research Centre on Earth Sciences.
[5]Quaid-i-Azam University, Department of Earth Sciences, Islamabad, Pakistan. E-mail: agulraiz@qau.edu.pk.

Recently, long-offset transient electromagnetic, electrical resistivity tomography (ERT), and ground-penetrating radar techniques have gained the most attention in near-surface investigations of groundwater-related hazards, e.g., water burst issues and coseismic liquefaction-induced deformation (Khan et al., 2018; Khan et al., 2019; Lee and Kim, 2019; Khan et al., 2021). Among passive geophysical methods, the horizontal-to-vertical spectral ratio (HVSR) survey (Nakamura, 1989) has been used extensively to assess the subsurface mechanical properties and, in particular, regional liquefaction hazard modeling due to its ease of use and its time- and cost-effectiveness (e.g., Singh et al., 2017; Qadri and Malik, 2021). The spectral features (e.g., amplitude and peak frequency) derived from HVSRs provide a fundamental basis for analysis of the site response in terms of their soil properties to ground movement. During the last few years, numerous site response studies have been conducted in various parts of Pakistan utilizing ambient noise data (Talha Qadri et al., 2017; Qadri and Malik, 2021). Similarly, in other parts of the world, HVSR and radon recordings have been used successfully in fault investigations (Chen et al., 2018; Cipta et al., 2020). To date, however, there is no systematic study reported in the literature demonstrating the impact of liquefaction-induced ruptures of seismic origin on the site response through HVSRs supported by ERT and radon data sets.

On 24 September 2019, the M_w 5.8 Mirpur earthquake produced mega-liquefaction spread over the entire area in the vicinity of the Mangla dam and along one of the oldest canal systems in Pakistan, the Upper Jhelum Canal (UJC), damaging residential dwellings, schools, mosques, and bridges and producing sand boils, land subsidence, and lateral spreading along both banks of the UJC. In this context, the Mirpur area calls for a systematic approach for better assessment of the coseismic liquefaction deformation for planning interventions aimed at hazard mitigation. In this work, we have used HVSR data to explain the site response supported by the ERT and radon measurements of the Mirpur area (Muhammad et al., 2020; Khan et al., 2021 and references therein). To the best of our knowledge, this study is the first to investigate the dynamic site response of the Mirpur earthquake-induced liquefaction ruptures using microtremor data in the epicentral area supported by the other in-situ measurements.

Geologic and seismological setting

The Indian Plate's subduction underneath Eurasia is responsible for generating major earthquakes of magnitude greater than M_w 7. Within this context, the Kashmir region in north Pakistan is one of the most active zones having high vulnerability to earthquakes. The 2005 Kashmir earthquake (about 100 km north of Mirpur) of M_w 7.6 claimed 90,000 lives, resulted in billions of dollars in loss to Pakistan's economy, and triggered several thousand landslides (ADB and WB, 2005; Khan et al., 2021 and references therein). In northern Pakistan, most of the historical major earthquakes have occurred in the décollement known as the Main Himalayan Thrust into which the causative Balakot Bagh Fault of the 2005 Kashmir earthquake is considered to sole out (Ali and Ali, 2020). Among these major seismic events, very few ruptured the surface of the Himalayan Frontal Thrust (HFT) (Mencin et al., 2016; Bilham, 2019). The HFT is one of the most important faults located in close proximity to the epicenter of the Mirpur earthquake (Figure 1a).

The Mirpur earthquake of M_w 5.8 caused 39 fatalities, injured more than 700, and caused damage to civil infrastructure (NDMA, 2019; USGS, 2019). It occurred in the Jhelum flood plain resulting in a maximum ground shake intensity of VI (Figure 2d; scale based on Worden et al., 2012). The geology is dominated by the Quaternary alluvial deposits overlying a liquefied sandy soil that played a key role in producing widespread liquefaction-induced effects. The liquefaction-induced long fractures (greater than 100 m) affected buildings, schools, the UJC, religious sites, and bridges, causing severe damage as a consequence of ground failures (Figures 1b–1e). The coseismic effects are observed within 6 km from the epicenter, including the most common ones within 50 m from the UJC (Figure 2b).

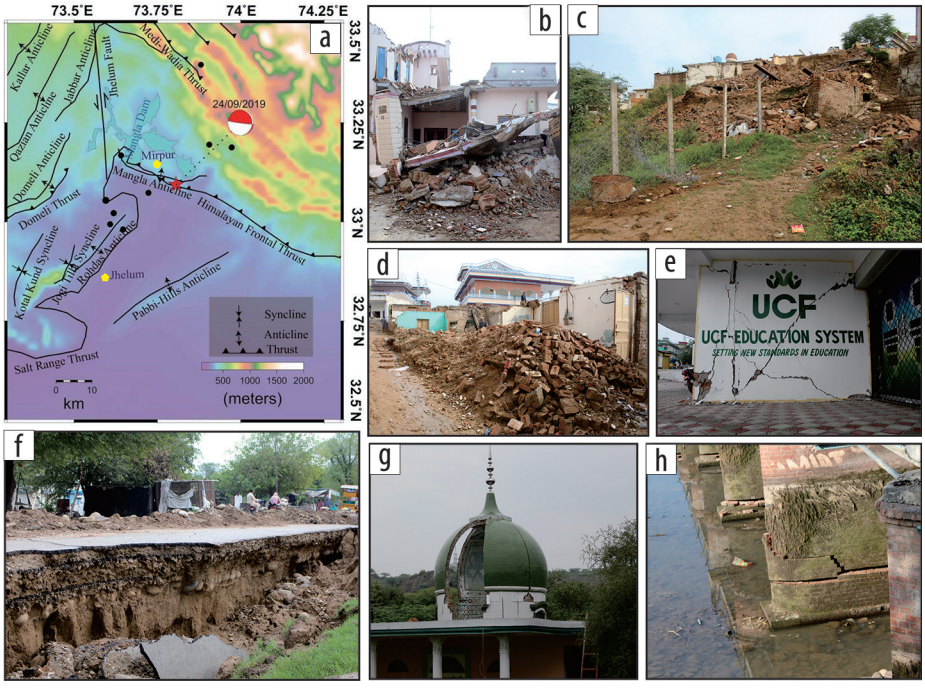


Figure 1. (a) Tectonic map of the study area (modified after Jayangondaperumal and Thakur, 2008). The red star denotes the epicenter of main shock associated with the earthquake and its focal plane mechanism solution (USGS, 2019), black dots denote aftershocks (M_w greater than 3.5) of the Mirpur earthquake (data source: www.isc.ac.uk, accessed 30 September 2019), heavy black line denotes the faults in the region, yellow polygon denotes major cities in the vicinity of the epicenter. Panels (b–d) show damage at site S3. Panels (e–h) show damage to school, bridge, UJC, and religious site.

HVSR

The passive seismic technique commonly known as the HVSR method (Nakamura, 1989) records the microtremor at a single station at which the

ground motion is amplified due to the high S-wave contrast between two material layers. The main use of the HVSR tool is to identify the resonance frequency and related amplitude to derive a relationship between the thickness of the softer layer (h) and the peak frequency (f) of the amplification function. Similarly, the peak amplitude (A) could be a rough indicator of whether stiffer layers are present in the subsurface. Using fundamental frequency f and thickness h, an estimate of the shear-wave velocity V_S is obtained using the following expression:

$$V_S = 4hf. \quad (1)$$

Thus, we can translate HVSR-frequency information into the depth-V_S domain when the layer depth is known to reconstruct the seismic stratigraphy (Castellaro and Mulargia, 2009). Hence, the spectral features (f, A) derived from HVSRs provide a fundamental basis for analysis of the site response to ground movement and thereby diagnostic key features of the site in terms of soil properties. In addition, different shapes of HVSR curves usually correspond to lateral heterogeneities in the subsoil (e.g., Matsushima et al., 2014).

Data collection

We collected HVSR data at 21 points at three sites — S1, S2, and S3 — including 16 points along AB, CD profiles across the ruptures at sites S1 and S2 (see Figures 4 and 5); only five points were randomly selected at site S3 where no liquefaction-induced ruptures were observed. Microtremor tests were performed in a systemic fashion at two selected sites S1 and S2 due to clear surface manifestations of the ruptures and availability of ERT and radon data for correlation and validation purposes. Ambient noise measurements were performed at a sampling rate of 128 Hz, each of 20 minutes along the AB and CD profiles and each of about 80 m long across the ground ruptures with four measuring points on each side and at a few random stations at site S3 (Figure 2b, Figures 3–5). The data were processed in accordance with

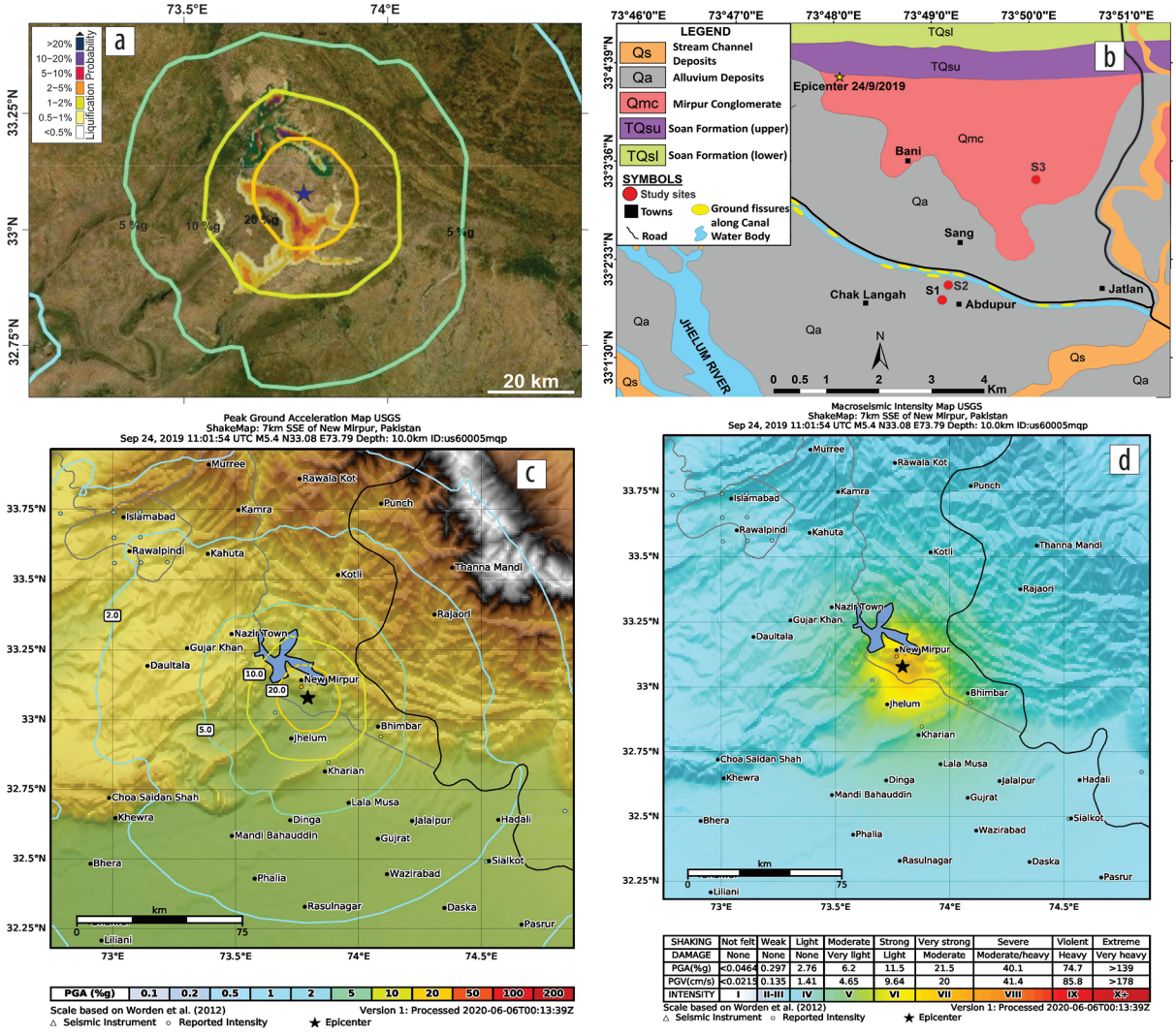


Figure 2. (a) Map showing locations of ERT (S1, S3, and S7) and sand blow (S4) field sites; (b) Surficial geologic map of the study area (modified after Arif et al., 2000). Surficial geologic deposits — Qs: unconsolidated clay, silt, sand, and gravel; Qa: uppermost soil; Qmc: poorly sorted conglomerate with sandy and clayey matrix; TQsu: gray clay, siltstone with conglomerate interbeds; TQsl: coarse-grained sandstone with interbedded claystone and conglomerate. Stratigraphic column — L1: uppermost soil; L2: loose sand and clay; L3: sand with gravel and clays; L4: gravel with sand. (c) Peak ground acceleration map. (d) Macroseismic intensity map.

SESAME (2004) criteria. The main purpose of microtremor data sets was to see the impact of distance from the main surface rupture and liquefaction-affected near surface on the seismic response. We have summarized the estimated spectral parameters and main characteristics of the ruptures at each site (see Table 1 and Figure 7).

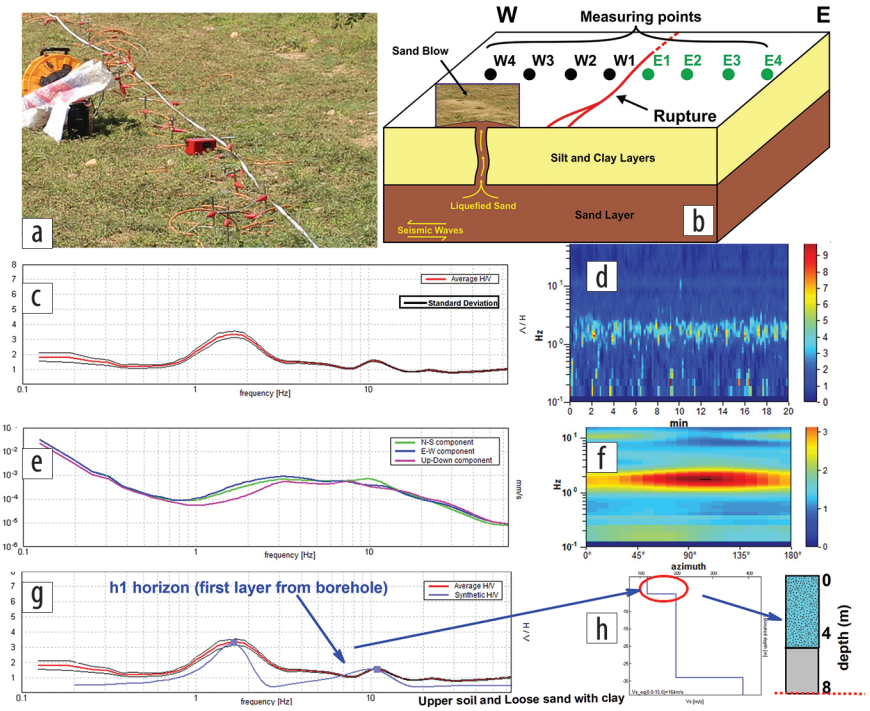


Figure 3. (a) HVSR profile layout across a liquefaction-induced rupture at site S1. (b) Schematic model showing data acquisition points (W1, W2, W3, W4) and (E1, E2, E3, E4) toward west and east, respectively. (c) A representative HVSR curve. The solid gray line represents standard deviations, while the continuous red line denotes average HVSR curve. (d) Time history. (e) Individual components. (f) Directionality at point W1 along AB profile. (g) The fitting between measured and theoretical HVSR curves. It is noted that high and low frequency peaks corresponding to shallowest (h1) and deeper stratigraphic horizons in measured HVSR curves (red solid line) are matched quite well with theoretical HVSR curves (blue solid line) and (h) 1D shear-wave velocity models obtained from forward modeling of HVSR curve.

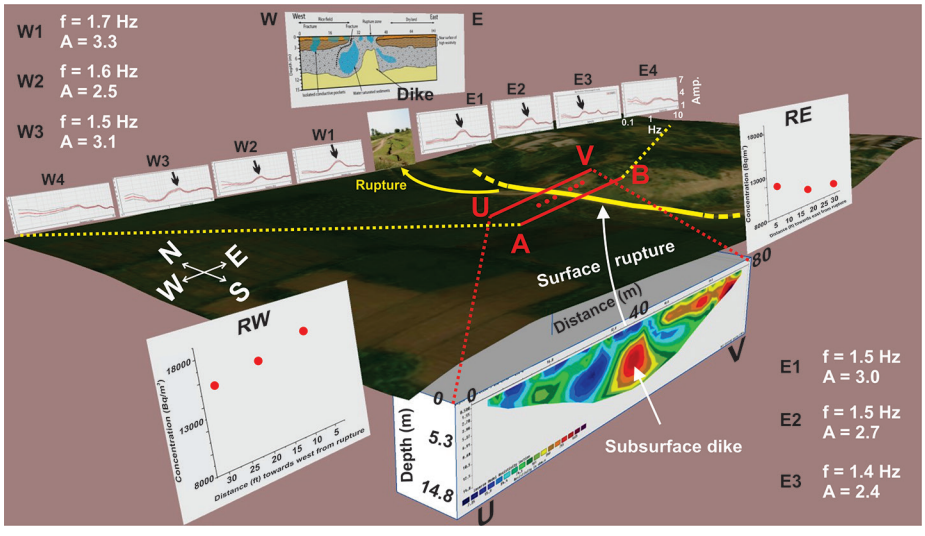


Figure 4. The layout of east–west-oriented HVSR profile (AB) at site S1 with a liquefaction-induced rupture; 3D schematic model to visualize the data acquisition points (E1, E2, E3, E4) and (W1 W2 W3, W4) on Google Earth imagery toward east and west, respectively. RE and RW show radon concentration at 10 ft on east and west sides. UV represent the ERT model. The field evidence of rupture and conceptual model are shown in the central part of the AB/UV transect.

Results

Amplitude and frequency content. Based on overall behavior displayed by HVSR curves in the entire area, ambient recordings can be analyzed roughly in two different frequency bands: (1) resonance frequency in the 1–3 Hz range and (2) multiple peaks of high frequency (greater than 3 Hz).

Figure 4 indicates that HVSR data collected at the farthest stations W3 and W4 on the western side of a coseismic liquefaction-induced rupture provided an unclear spectral pattern. Such spectral trends could be associated with the reworked soil and lateral heterogeneities in the near surface due to the presence of a rice field and small-scale liquefaction-induced discontinuities. Moving toward the main rupture, we observed well-established frequency peaks with a change in both amplitude and frequency for the latter at stations W2 and W1. The amplitude and frequency values increased from 2.5 to 3.3 and approximately 1.5 to 1.7 Hz, respectively. Similar behavior could be seen eastward in relation to spatial change in distance from the rupture. These spectral trends along the east-west profile are attributed to the liquefaction-induced rupture and agree with the ERT and radon recordings along the same AB profile of HVSR data. The detection of well-defined resonance peaks at stations adjacent to the rupture (W1 and E1) can be explained further by high concentration of more than 15,000 Bq/m^3 and more than 8000 Bq/m^3 of radon in the soil as we move toward the rupture on the western and eastern parts, respectively. A high resistivity anomaly indicating sand intrusion in the central part of the inverted ERT model along the UV profile provides additional evidence to support the occurrence of liquefaction, and hence rupture, at the ground surface.

Figure 5 shows that ambient noise data on the westernmost point (W4) display almost a flat curve having no frequency peaks that could be related to the stratigraphic contacts. At station W3, very broad frequency peaks of 0.4 and 2 Hz are detected. The low-frequency unclear peak (0.4 Hz) may correspond to the fractured shallow subsurface as a consequence of the groundwater movement and transportation of liquified sand toward ground

surface. The second peak at about 2 Hz is the most common spectral feature observed at all sites S1, S2, and S3 with a high frequency spectrum in the 1.6–3 Hz range. Moving toward the rupture, at stations W2 and W1, spectral peaks of approximately 2 Hz frequency are detected, with a slight amplification at the latter one. The gradual increase in both frequency and amplitude (1.5–2.0 Hz and 2.5–5.0, respectively) toward the rupture can be explained by the increasing influence of the liquefaction-induced rupture on the HVSR characteristics. The absence of any HVSR peak indicates very weak impedance contrast beneath a particular station (D'Amico et al., 2008). Such a flat HVSR curve on the east side at station E4 shows no distinct feature which could be attributed to a geologic interface and/or structural target of interest in the context of coseismic deformation. However, closer to the ground rupture, a stable frequency peak of about 1.5 Hz and high-frequency peaks of greater than 3 Hz can be observed at points E3 and E2. An increase in the amplification (3.5 times) could be seen at station E1 near the rupture when compared to the station E4 located 40 m from the rupture.

Collectively, a distinct drop in the amplification values of HVSR spectral ratios is noticed with an increase in the distance from the rupture in addition to the spatial change in the resonance frequencies on either side of the coseismic feature. We suggest that earthquake-induced liquefaction ruptures have strongly influenced the behavior of HVSRs as reflected by the dynamic patterns of the amplification and resonance frequencies. This hypothesis is supplemented by the field observations and found in agreement with the correlateable trends of the ERT and radon data measurements.

The Mirpur area in the Kashmir region of northern Pakistan is located in one of the most seismologically active environments in the world. In such areas, the structural vulnerability of existing residential buildings and/or other civil infrastructure subjected to an earthquake is generally related to the main structural members and local site conditions in controlling the distribution of damage. The impedance contrasts at shallow seismic units characterized by low and high S-wave velocities may result in the strong resonance and amplification phenomena. The reconstruction of this natural amplification occurring within the subsoil are of utmost importance in the Mirpur area in order to highlight the zones prone to high amplification. At a given site, an amplified frequency close to a building would lead to a resonance effect that increases the risk of structural damage (e.g., Mucciarelli and Monachesi, 1998; Mucciarelli et al., 2011). Hence, we performed HVSR surveys at five stations at site S3 adjacent to the collapsed and/or heavily damaged buildings in the Sang Kikri village.

Table 1. Estimated spectral parameters at each site.

Site #	HVSR profile	HVSR profile length (m)	Fundamental frequency (Hz)	Amplification	Average shear-wave velocity V_{S15} (m/s)
S1	AB	80	1.4–1.7	2.4–3.3	164–191
S2	CD	80	1.5–2.0	3.0–5.0	157–199
S3	-	-	2.9–3.4	3.6–4.1	193–326

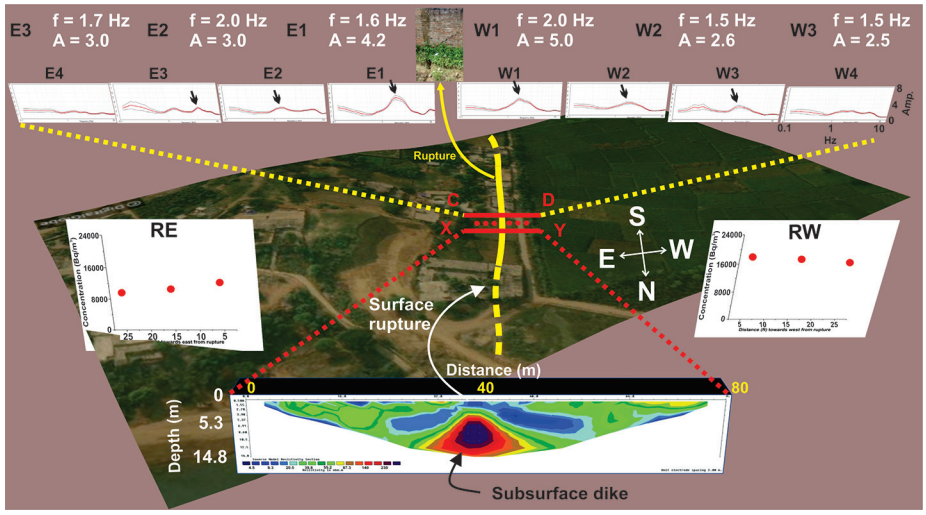


Figure 5. The layout of east–west-oriented HVSR profile (CD) at site 2 with a liquefaction-induced rupture; 3D schematic model to visualize data acquisition points (E1, E2, E3, E4) and (W1 W2 W3, W4) on the Google Earth imagery toward east and west, respectively. RE and RW show radon concentration at 10 ft on east and west sides. XY represents the ERT model. The field evidence of rupture is shown in the central part of the CD/XY transect.

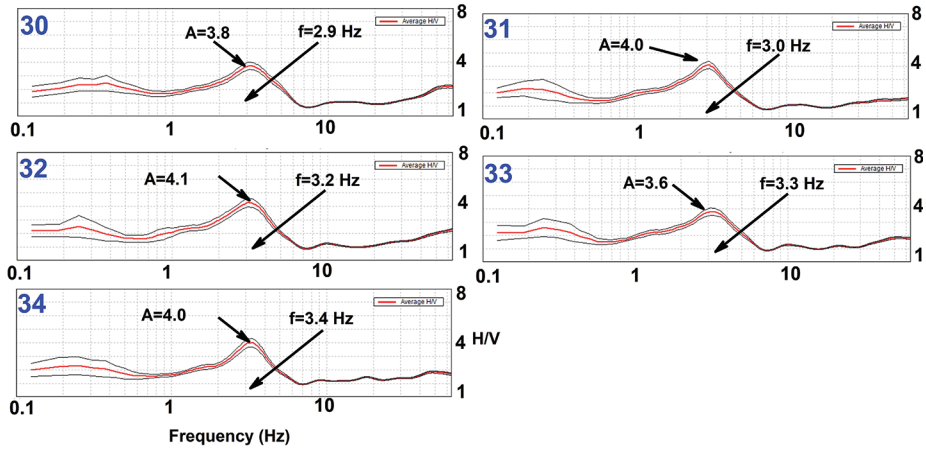


Figure 6. Results of HVSR stations at site S3. The solid gray lines show standard deviations, while continuous red lines denote the average HVSR curve.

These HVSR stations were not located across the rupture and hence do not represent any influence of coseismic surface features on the spectra at site S3. The fundamental frequency at the two sites S1 and S2 along the Jhelum River was in the 1.5–2 Hz range, while it was about 3 Hz at site S3. The relatively consistent frequency peaks of 3 Hz with stable amplitudes of about 4 units, unlike other sites S1 and S2 with decaying amplitudes and relatively lower frequencies, may be related to the combined effect of spatial change in alluvium thickness along the Jhelum River, the impact of main hydrological features (Jhelum River and UJC), distance from the epicenter, and coseismic liquefaction manifestations on the ground surface. It is important to mention that residential buildings suffered severe to partial damage (Figures 1b–1e). It is likely that the amplified frequencies at site 3 may have reached the value close to that of the buildings and may have caused a resonance effect. To establish a link between the damage distribution/intensity and ground vulnerability, dense sampling of HVSRs is mandatory at site S3.

Impact of spatial change in distance from the rupture on the dynamic site response. The spatial change in the main spectral characteristics (amplitude and frequency) and shape of the HVSR curves was detected on each side of the ground rupture at sites S1 and S2 (Figure 7). On the west and east sides, the amplification factor showed an increasing trend toward the rupture and drops to its minimum value of approximately 2.3 at 30 m away from the rupture on the eastern part. Similarly, an increasing trend of peak frequency with maximum values at 10 m on each side adjacent to the ground rupture indicates the range of its influence on the dynamic response at site S1. Generally, the decreasing values of amplification factor and resonance frequency away from the rupture is in agreement with the radon concentration measurements with respect to the rupture and may possibly conclude on the influence range of coseismic liquefaction-induced rupture. It marks the distance (30 m) over which the frequency and amplification factors drop to their minimum values of 1.4 Hz and 2.4 on the east side, and 1.5 Hz and 3.1 on the west side, respectively, at site S1. In addition, the influence exerted by the near-surface discontinuities as a consequence of liquefaction-induced disruption of soil layers on HVSR behavior cannot be excluded, as indicated by the ERT model. In the case of site S1, the rice field on the west side could have altered the site response at distant points (more than 25 m) due to agricultural practices as compared to the east section, which was of a comparatively dry and stiff nature. At the farthest points (more than 30 m) from the rupture, HVSR

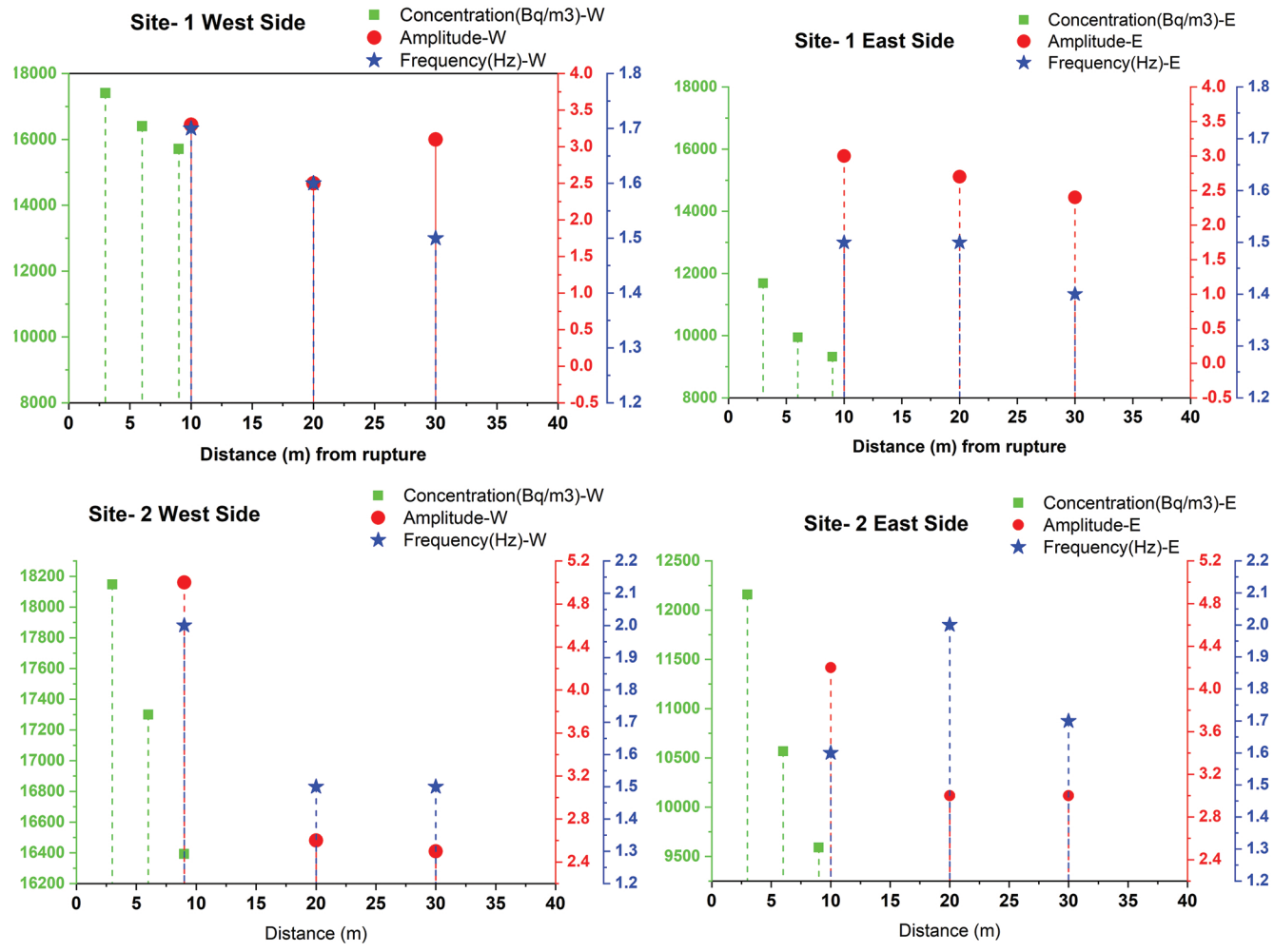


Figure 7. HVSR frequency and amplification factor versus distance from rupture and its correlation with radon concentration at each side of sites S1 and S2.

curves were almost flat with no defined peaks that could be explained within the geologic context. However, the microtremor recordings at stations adjacent to ruptures showed relatively well-established frequency peaks with a slight change in frequency in addition to seismic amplification. At 10 m from rupture, the amplification factor along the AB profile reaches maximum values of 3.3 and 3.0 on the western and eastern sections, respectively, which corresponds to the higher radon concentrations at 3.08 m at the closest sampled points to the rupture at site S1.

Site S2 displayed a consistent increase in amplification factor and resonance frequency with decrease in distance from the rupture with values of 5.0 and 2 Hz at 10 m, and of 2.5 and 1.5 Hz at 30 m, respectively, on the west side. The considerable increase in amplification factor at the nearest point could be the result of coseismic rupture. Likewise, a consistent increase in amplification from 3.0 to 4.2 with spatial change (30 to 10 m) in distance was observed on the east side of the rupture. However, the peak frequency was not influenced in a similar way while moving toward the rupture. A strong influence of coseismic rupture could be seen on the shape of the HVSR curves characterized by a flat response to a clear peak while moving from the farthest station at 40 m to the closest one at 10 m.

Generally, both sites S1 and S2 showed a spatial change in the shape, amplification factor, and peak frequency of HVSR curves that we suggest to be controlled predominantly by the rupture. This dynamic seismic response of sites, supported by the radon data set, was seen in the range of influence of about 40 m on each side of the earth rupture. Ambient noise recordings at five stations showed a consistent HVSR behavior with amplification factor of 3.0 and frequency of about 3 Hz on site S3. The HVSR measurements were not acquired across a particular rupture due to unavailability of a surface rupture.

Retrieval of 1D V_S profiles. To construct a multilayer V_S-depth model (i.e., more than two layers), we have adopted the popular approach that only requires information about first layer thickness (h1) of subsoil stratigraphy (Castellaro and Mulargia 2009; Ambrish Kumar and Kumar, 2018). The borehole B1, located in proximity to site S1, extended to a depth of 8 m (Figure 3). The stratigraphic layer h1 was found to be 5 m of loose sand and clays/silt. During synthetic HVSR modeling, we used the most superficial layer thickness (h1) from the nearby borehole and ERT inverted model as a constraint fit. The fitting of recorded HVSR curves with synthetic HVSR curves was carried out by using a forward-modeling module implemented in Grilla software through random perturbation. During the iteration process, the search for an optimal solution continues until a good match between theoretical and observed HVSR curves is found. At this point, the input subsoil model and selected V_S produces a site-specific 1D V_S-depth profile. A schematic diagram summarizes the stepwise procedure in the following.

The misfit between the synthetic and observed curves usually is quantified as standard deviation. In this work, the standard deviations in the HVSR peak frequencies derived from the curves were found to be ±1 and shown as solid gray lines, while average HVSR curves are shown as continuous red lines (Figures 3 and 6). The over- and underestimation of synthetic curves may lead to

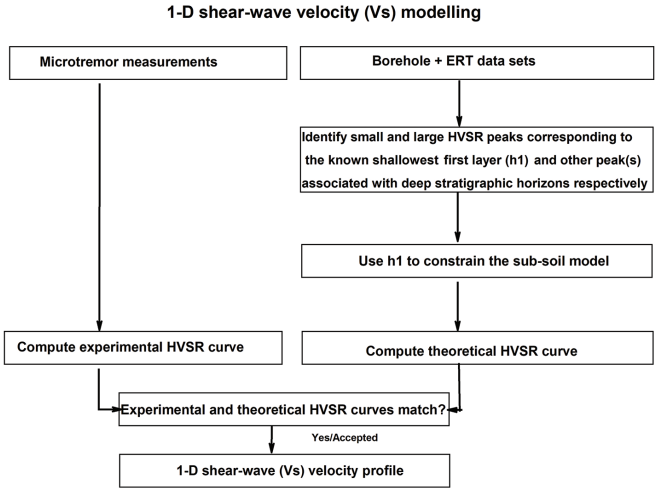


Figure 8. A schematic diagram showing the stepwise procedure for finding multilayer 1D shear-wave velocity model from HVSR curves and borehole data.

10%–15% deviations between calculated shear-wave velocity values from HVSR forward modeling and field data (Singh et al., 2020). The study sites were located within 5 km of the main Mangla–Jatlan road, so HVSR measurements were performed during early morning to avoid obvious vibration sources and to minimize some of the random noise contamination. Besides field measurements, an uncertainty at different stages, such as the processing stage (e.g., choice of model), framework, and interpretation of the HVSR-derived V_S profile could bias the site-response analysis. Thus, we adopted a multiproxy approach by using supplementary information from the ERT, radon, and field surveys at the studied sites to reduce the uncertainties associated with the 1D HVSR method. Constrained V_S estimates of reasonable accuracy were obtained with which shear-wave velocity structures can be retrieved from observed HVSRs. The results suggest, therefore, an application of the method for a site-specific analysis of coseismic liquefaction hazard.

Based on the V_S trends, such 1D inverted models represent the near-surface subsoil condition at the local site, which in turn could be linked to the liquification potential. For instance, Stokoe et al. (1988) reported that the sandy layer with V_S less than or equal to 180 m/s is susceptible to liquefaction phenomenon. Contrary to National Earthquake Hazards Reduction Program criteria for site classification based on V_{S30}, we derived site-specific V_{S15} profiles to indicate the vulnerability of local soil to coseismic liquefaction hazard in the upper 15 m, because of well-established radon concentration patterns in the soil, surface manifestations of liquefaction-induced features, and especially their detection on the ERT sections within 15 m depth. In addition, this depth range covers the foundations of civil structures, the groundwater table, and the entire soil profile for crop yield and thereby is strongly relevant to societal health, food security, and public safety.

Inversion results demonstrated that synthetic HVSR curves agreed with the measured HVSR ratio, while slight overprediction at some stations could be associated to the strong V_S contrasts than the real ground conditions (Souriau et al., 2011). In general, inverted models consisting of three to four soil layers showed an

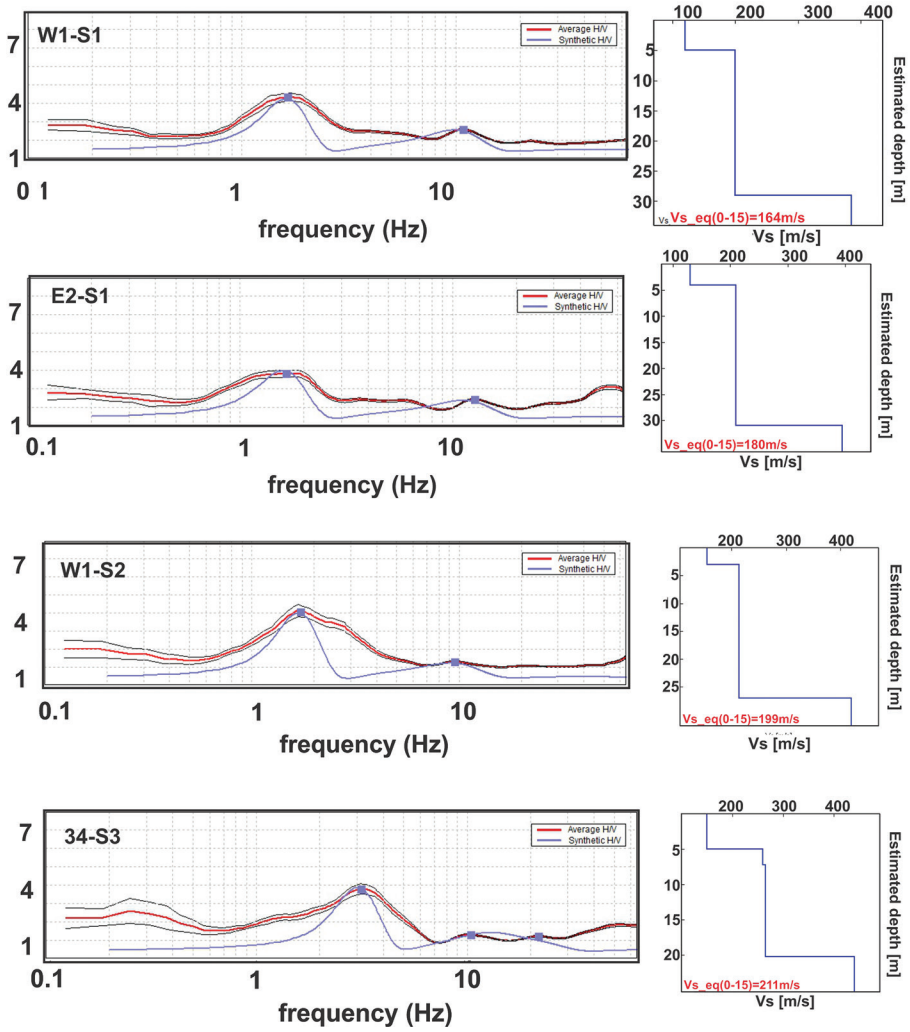


Figure 9. V_S-depth profiles at sites S1, S2, and S3. W and E denote HVSR stations on the west and east sides with respect to the rupture, and S represents site. The red, black, and blue lines represent observed HVSR ratio, standard deviation, and synthetic HVSR curve, respectively. Inversion results (V_S-depth profiles) against each HVSR station are shown in the four squares on the right of the figure.

increasing V_S trend against depth (Figure 9). At site S1, we observed low velocities with V_{S15} ranging from 164 to 191 m/s, and V_S of less than 180 m/s in the uppermost loose soil of 5 m thick intervals on both sides of the liquefaction-induced rupture at stations W1-S1, E1-S1, W2-S1, and E2-S1. Similarly, low velocity values (V_{S15} of about 157 m/s and V_S less than 180 m/s) were obtained in the top loose soil across the coseismic rupture at site S2. Both sites displayed a variation in the V_S profiles in terms of lower values that may confirm the presence of liquefaction-induced rupture as a consequence of the Mirpur earthquake and soil susceptibility to liquefaction and reliquefaction in the near surface due to existing fractures in the top soil layers in case of future earthquakes. The V_{S15} values at site S3 range from 193 to 326 m/s, whereas V_S is less than 180 m/s, which confirms that the shear-wave velocities are in the vulnerable range to coseismic liquefaction. Overall, the liquefaction-affected area is characterized by V_{S15} ranging from 164 to 326 m/s and V_S less than 180 m/s, which, based on criteria defined by Stokoe et al. (1988), indicates that all of the studied sites are potentially susceptible to liquefaction hazard. However, in the near future, these preliminary results will be confirmed through detailed district-level seismic microzonation investigations of the study area.

Discussion

Field observations, soil radon measurements, and subsurface ERT imaging of liquefaction-induced deformation. The surface manifestations of coseismic liquefaction in the field include sand blows, subsidence and extrusion of sediments above the earth's surface, and ground ruptures (Figures 1 and 3). Radon gas naturally occurs in the earth's crust and diffuses into the soil and groundwater. The highly soluble nature of radon gas makes the groundwater system a host enriched with its concentration. The enhanced pore water pressure triggered by the Mirpur earthquake resulted in movement of groundwater as well as transportation of liquified sand from deeper layers toward the ground surface. Having said that, the radon gas may have been diffused through the pore water and thereby traveled along liquified material toward the near-surface soil layers during liquefaction. The higher radon concentrations in the soil measured across the ruptures at sites S1 and S2 showed increasing concentration trends with decreasing distance from the rupture on each side (Figures 3 and 4). High-resolution ERT inversion results revealed fracture sets, intrusion of liquified sand plugs, and very conductive lenses. All these results confirm that the Mirpur earthquake-induced liquefaction hazard caused severe damage to the ground surface as well as the near surface. This is shown by schematic representation in pre- and post-Mirpur-earthquake scenarios (Figure 10).

Implications of coseismic liquefaction hazard and its influence on HVSR behavior. The dynamic characteristics of HVSR curves (flat to broad to well-defined single-frequency peaks) along an 80 m profile may further confirm the magnitude of liquefaction-induced deformation in the area (Figures 4 and 5). The results demonstrated that the coseismic rupture caused seismic amplification at adjacent stations, while distant HVSR points displayed little or no such phenomenon that confirms the influence of coseismic features on the site response. The variability in the HVSR ratio in terms of peak frequency and their shape indicate the impact of surface ruptures and deformed character of the near surface in the earthquake-affected area. Interestingly, the spatial change in spectral features at a short distance along a profile of 80 m length concludes on the dynamic response of studied sites following the Mirpur earthquake by altering the soil properties

and thereby site response. Furthermore, the U.S. Geological Survey's shake maps for the Mirpur earthquake reveal that all surface deformation sites are located within the core of the maximum recorded ground shaking (Figures 2a and 2d).

We suggest that overall behavior of the HVSR curves was controlled by the shallow structural features in the subsurface as well as the coseismic effects on the ground surface. These underground liquefaction features (clay lenses, fractures, and sand plugs) detected on the ERT may have significant influence on the HVSR trends due to their presence in the upper 0–15 m. This depth range covers the thickness of soft deposits above the bedrock to which HVSRs show more sensitivity. The systematically acquired microtremor measurements could be used to assess unknown sites with no surface rupture manifestations in the orientation of the main ground rupture trace. In addition, joint use of radon and HVSR could help detect buried faults by performing dense ambient noise recordings in the vicinity of populated cites of the seismically active Kashmir valley as suggested by Rossetto and Peiris (2009). Such investigations should be conducted on a priority basis in tectonically active areas where no site information has been considered in the past while designing buildings.

Collectively, the Mirpur earthquake produced long fractures (greater than 100 m) and widespread damage to bridges, agricultural fields, all types of buildings, water supply networks, and roads that call for urgent and detailed soil-liquefaction hazard assessment that may provide useful information on the seismic

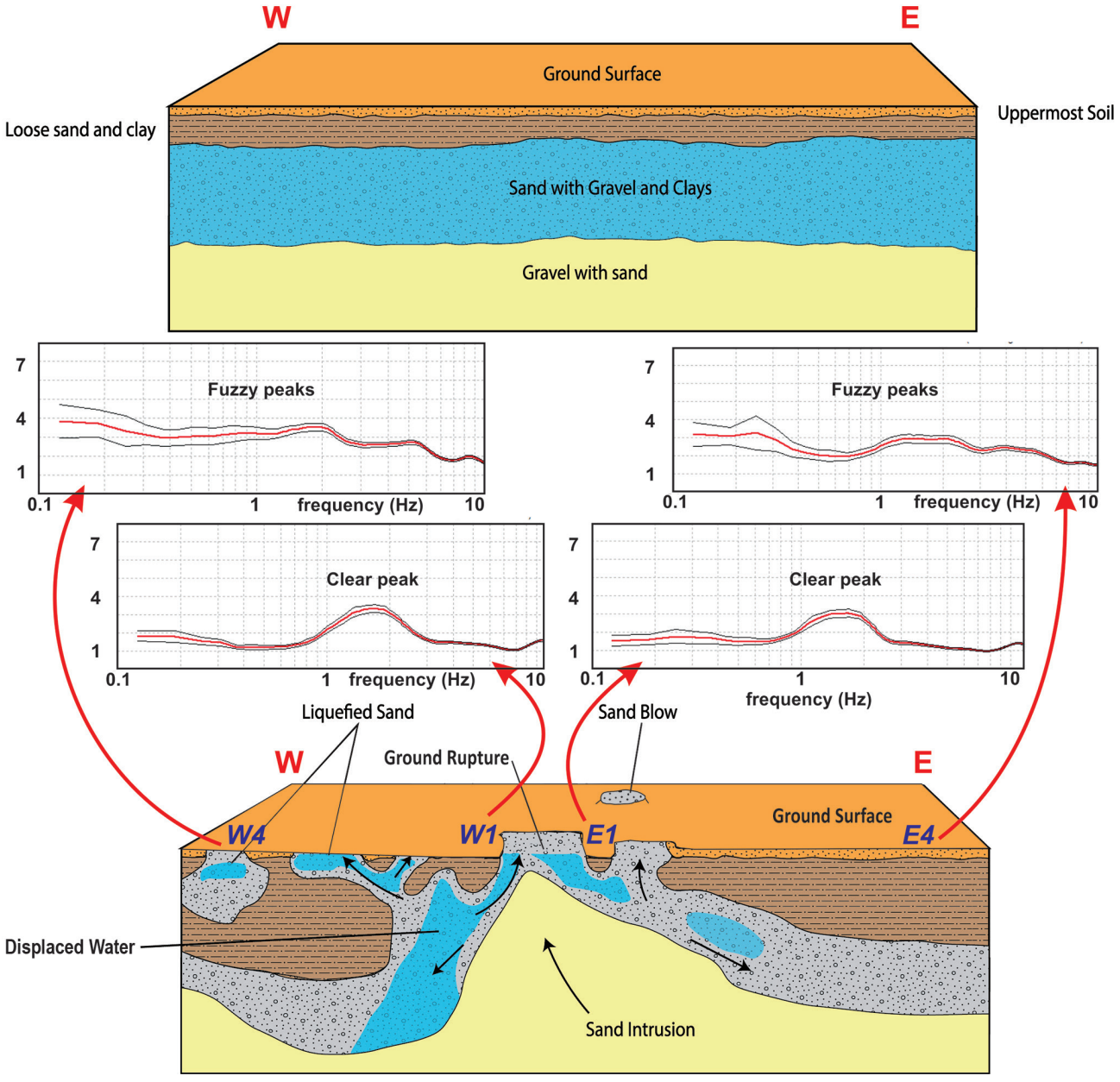


Figure 10. Schematic representation of pre- and post-Mirpur-earthquake-triggered liquefaction hazard and associated ground rupture, eruption of sand, and other coseismic features based on interpretation of geologic and geophysical data. The short and long red arrows show the closest and farthest seismic stations, respectively, with respect to the coseismic rupture (modified after Khan et al., 2021).

vulnerability of the existing infrastructure and further guide in the seismic design of new constructions.

Conclusions

HVSR-derived quantified parameters (resonance frequency, amplification factor, and V_S values) helped determine the site effects in the coseismic liquefaction-affected Mirpur area. Systematically collected HVSRs across the coseismic ruptures at two selected sites S1 and S2 provided quantifiable observations of seismic wave amplification in the soft Quaternary deposits prevalent throughout the Mirpur area. Different patterns of resonance frequency confirm the influence of liquefaction-induced features on the behavior of seismic response. The correlated trends of intermethod comparisons, i.e., geophysical (ERT) and geochemical (radon) data sets, further validate the microtremor results by determining the dynamic response characteristics of ruptures at sites S1 and S2. The low shear-wave velocities as well as the increasing concentrations of radon in the soil and enhanced amplification closer to the rupture document the influence of site-specific coseismic liquefaction deformation. Similarly, the stable frequency and amplitude values and severe damage to the buildings on the liquified soil may provide a clue of occurrence of resonance phenomenon that could have enhanced the seismic vulnerability of infrastructure at site S3. However, the preliminary results indicate a strong need for a detailed investigation that could further explain these observations by evaluating ground vulnerability based on microtremor information. The successful application of the time- and cost-effective HVSR method provides valuable information that can help with seismic hazard analysis and mitigation in an area where buildings in close proximity to key critical structures (the UJC and Mangla dam) have been constructed in the past with no seismic concept. Based on quantified site effects and retrieved V_S-depth profiles, we suggest that urban planners should consider the results outlined in this study in future urban development projects. TLE

Data and materials availability

The data can be obtained from the corresponding author upon reasonable request.

Corresponding author: myouniskhan@uop.edu.pk

References

ADB and WB, 2005, Pakistan 2005 earthquake: Preliminary damage and needs assessment: Asian Development Bank and World Bank.

Ali, U., and S. A. Ali, 2020, Comparative response of Kashmir Basin and its surroundings to the earthquake shaking based on various site effects: Soil Dynamics and Earthquake Engineering, **132**, 106046, https://doi.org/10.1016/j.soildyn.2020.106046.

Alvarez, W., 2010, Protracted continental collisions argue for continental plates driven by basal traction: Earth and Planetary Science Letters, **296**, no. 3–4, 434–442, https://doi.org/10.1016/j.epsl.2010.05.030.

Ambrish Kumar, M., and P. Kumar, 2018, Site characterization in Kangra Valley (NW Himalaya, India) by inversion of H/V spectral ratio from ambient noise measurements and its validation by multichannel analysis of surface waves technique: Near Surface Geophysics, **16**, no. 3, 314–327, https://doi.org/10.3997/1873-0604.2018008.

Arif, M., S. H. Hussain, R. Khan, and A. Hussain, 2000, Geological map of the Mirpur area, Mirpur and Bhimber districts, AJK and parts of the Gujrat and Jhelum districts, Punjab, Pakistan: Geological Survey of Pakistan, Geological Map Series, **VI**, no. 29.

Bilham, R., 2019, Himalayan earthquakes: A review of historical seismicity and early 21st century slip potential: Geological Society, London, Special Publications, **483**, 423–482, https://doi.org/10.1144/SP483.16.

Borcherdt, R. D., and G. Glassmoyer, 1992, On the characteristics of local geology and their influence on ground motions generated by the Loma Prieta earthquake in the San Francisco Bay region, California: Bulletin of the Seismological Society of America, **82**, no. 2, 603–641.

Castellaro, S., and F. Mulargia, 2009, VS 30 estimates using constrained H/V measurements: Bulletin of the Seismological Society of America, **99**, no. 2A, 761–773, https://doi.org/10.1785/0120080179.

Chen, Z., Y. Li, Z. Liu, J. Wang, X. Zhou, and J. Du, 2018, Radon emission from soil gases in the active fault zones in the capital of China and its environmental effects: Scientific Reports, **8**, 16772, https://doi.org/10.1038/s41598-018-35262-1.

Cipta, A., A. Rudyanto, H. Afif, R. Robiana, A. Solikhin, A. Omang, and S. Hidayati, 2020, Unearthing the buried Palu-Koro Fault and the pattern of damage caused by the 2018 Sulawesi earthquake using HVSR inversion: Geological Society, London, Special Publications, **501**, 185–203, https://doi.org/10.1144/SP501-2019-70.

D'Amico, V., M. Picozzi, F. Baliva, and D. Albarello, 2008, Ambient noise measurements for preliminary site-effects characterization in the urban area of Florence, Italy: Bulletin of the Seismological Society of America, **98**, no. 3, 1373–1388, https://doi.org/10.1785/0120070231.

Galli, P., 2000, New empirical relationships between magnitude and distance for liquefaction: Tectonophysics, **324**, no. 3, 169–187, https://doi.org/10.1016/S0040-1951(00)00118-9.

Galli, P., S. Castenetto, and E. Peronace, 2012, The MCS macroseismic survey of the Emilia 2012 earthquakes: Annals of Geophysics, **55**, no. 4, https://doi.org/10.4401/ag-6163.

Jayangondaperumal, R., and V. C. Thakur,2008, Co-seismic secondary surface fractures on southeastward extension of the rupture zone of the 2005 Kashmir earthquake: Tectonophysics, **446**, no. 1–4, 61–76, https://doi.org/10.1016/j.tecto.2007.10.006.

Jefferies, M., and K. Been, 2015, Soil liquefaction: A critical state approach: CRC Press, https://doi.org/10.1201/b19114.

Khan, M. Y., K. Rehman, W. Ali, S. A. Turab, K. Latif, and S. Iqbal, 2019, Characterization of ground penerating radar (GPR) wave response in shallow subsurface for forensic investigation in controlled environment: Journal of Himalayan Earth Sciences, **52**, no. 1, 58–64.

Khan, M. Y., S. A. Turab, M. S. Riaz, E. A. Atekwana, S. Muhammad, N. A. Butt, S. M. Abbas, W. A. Zafar, and L.O. Ohenhen, 2021, Investigation of coseismic liquefaction-induced ground deformation associated with the 2019 M_w 5.8 Mirpur, Pakistan, earthquake using near-surface electrical resistivity tomography and geological data: Near Surface Geophysics, **19**, no. 2, 169–182, https://doi.org/10.1002/nsg.12148.

Khan, M. Y., G.-Q. Xue, W.-Y. Chen, and H.-S. Zhong, 2018, Analysis of long-offset transient electromagnetic (LOTEM) data in time, frequency, and pseudo-seismic domain: Journal of Environmental and Engineering Geophysics, **23**, no. 1, 15–32, https://doi.org/10.2113/JEEG23.1.15.

Lee, Y. H., and S.-S., Kim, 2019, Imaging of liquefaction features using ground penetrating radar in Pohang, South Korea: EGU General Assembly, Geophysical Research Abstracts, **21**.

Matsushima, S., T. Hirokawa, F. De Martin, H. Kawase, and F. J. Sánchez-Sesma, 2014, The effect of lateral heterogeneity on horizontal-to-vertical spectral ratio of microtremors inferred from observation and synthetics: Bulletin of the Seismological Society of America, **104**, no. 1, 381–393, https://doi.org/10.1785/0120120321.

Mencin, D., R. Bendick, B. N. Upreti, D. P. Adhikari, A. P. Gajurel, R. R. Bhattarai, H. R. Shrestha, et al., 2016, Himalayan strain reservoir inferred from limited after slip following the Gorkha earthquake: Nature Geoscience, **9**, 533–537, https://doi.org/10.1038/ngeo2734.

Mucciarelli, M., M. Bianca, R. Ditommaso, M. Vona, M. R. Gallipoli, A. Giocoli, S. Piscitelli, E. Rizzo, and M. Picozzi, 2011, Peculiar earthquake damage on a reinforced concrete building in San Gregorio (L'Aquila, Italy): Site effects or building defects?: Bulletin of Earthquake Engineering, **9**, 825–840, https://doi.org/10.1007/s10518-011-9257-3.

Mucciarelli, M., and G. Monachesi, 1998, A quick survey of local amplifications and their correlation with damage observed during the Umbro-Marchesan (Italy) earthquake of September 26, 1997: Journal of Earthquake Engineering, **2**, no. 2, 325–337, https://doi.org/10.1080/13632469809350325.

Muhammad, S., R. Ullah, S. A. Turab, M. Y. Khan, N. U. Khattak, and M. A. Khan, 2020, Radon concentration in drinking water and soil after the September 24, 2019, Mw 5.8 earthquake, Mirpur, Azad Jammu, and Kashmir: An evaluation for potential risk: Environmental Science and Pollution Research International, **27**, no. 26, 32628–32636, https://doi.org/10.1007/s11356-020-09589-0.

Nakamura, Y, 1989, A method for dynamic characteristics estimation of subsurface using microtremor on the ground surface: Railway Technical Research Institute, Quarterly Reports, **30**.

NDMA, 2019, NDMA situation report 18 — Mirpur Earthquake 2019, www.ndma.gov.pk.

Orense, R., M. Pender, and L. Wotherspoon, 2012, Analysis of soil liquefaction during the recent Canterbury (New Zealand) earthquakes: Geotechnical Engineering Journal of the SEAGS and AGSSEA, **43**, 8–17.

Owen, G., and M. Moretti, 2011, Identifying triggers for liquefaction-induced soft-sediment deformation in sands: Sedimentary Geology, **235**, no. 3–4, 141–147, https://doi.org/10.1016/j.sedgeo.2010.10.003.

Owen, G., M. Moretti, and P. Alfaro, 2011b, Recognising triggers for soft-sediment deformation: Current understanding and future directions: Sedimentary Geology, **235**, no. 3–4, 133–140, https://doi.org/10.1016/j.sedgeo.2010.12.010.

Qadri, S. M. T., and O. A. Malik, 2021, Establishing site response-based micro-zonation by applying machine learning techniques on ambient noise data: A case study from Northern Potwar Region, Pakistan: Environmental Earth Sciences, **80**, https://doi.org/10.1007/s12665-020-09322-7.

Rossetto, T., and N. Peiris, 2009, Observations of damage due to the Kashmir earthquake of October 8, 2005 and study of current seismic provisions for buildings in Pakistan: Bulletin of Earthquake Engineering, **7**, 681–699, https://doi.org/10.1007/s10518-009-9118-5.

SESAME, 2004, Guidelines for the implementation of the H/V spectral ratio technique on ambient vibrations: Measurements, processing and interpretation: European Commission, http://sesame.geopsy.org/SES_Reports.htm, accessed 14 July 2021.

Shafique, M., and M. Y. Khan, 2015, Earthquake hazards and risk mitigation in Pakistan, *in* A. U. Rahman, A. N. Khan, and R. Shaw, eds., Disaster risk reduction approaches in Pakistan: Springer, 101–117, https://doi.org/10.1007/978-4-431-55369-4_5.

Shao, Z.-F., J.-H. Zhong, J. Howell, B. Hao, X.-W. Luan, Z.-X. Liu, W.-M. Ran, et al., 2020, Liquefaction structures induced by the M5.7 earthquake on May 28, 2018 in Songyuan, Jilin Province, NE China and research implication: Journal of Palaeogeography, **9**, article no. 3, https://doi.org/10.1186/s42501-019-0053-3.

Singh, A. P., B. Sairam, V. Pancholi, S. Chopra, and M. Ravi Kumar, 2020, Delineation of thickness of intrabasaltic rocks beneath the Deccan volcanic province of western India through microtremor analysis: Soil Dynamics and Earthquake Engineering, **138**, 106348, https://doi.org/10.1016/j.soildyn.2020.106348.

Singh, A. P., A. Shukla, M. Ravi Kumar, and M. G. Thakkar, 2017, Characterizing surface geology, liquefaction potential, and maximum intensity in the Kachchh seismic zone, Western India, through microtremor analysis: Bulletin of the Seismological Society of America, **107**, no. 3, 1277–1292, https://doi.org/10.1785/0120160264.

Souriau, A., E. Chaljub, C. Cornou, L. Margerin, M. Calvet, J. Maury, M. Wathelet, et al., 2011, Multimethod characterization of the French-Pyrenean valley of Bagnères-de-Bigorre for seismic-hazard evaluation: Observations and models: Bulletin of the Seismological Society of America, **101**, no. 4, 1912–1937, https://doi.org/10.1785/0120100293.

Stokoe, K. H., J. M. Roesset, J. G. Bierschwale, and M. Aouad, 1988, Liquefaction potential of sands from shear wave velocity: Proceedings of Ninth World Conference on Earthquake Engineering, **3**, 213–218.

Takahama, N., T. Otsuka, and B. Brahmantyo, 2000, A new phenomenon in ancient liquefaction — The draw-in process, its final stage: Sedimentary Geology, **135**, no. 1–4, 157–165, https://doi.org/10.1016/S0037-0738(00)00069-5.

Talha Qadri, S. M., M. A. Islam, M. R. Shalaby, K. R. Khattak, and S. H. Sajjad, 2017, Characterizing site response in the Attock Basin, Pakistan, using microtremor measurement analysis: Arabian Journal of Geosciences, **10**, https://doi.org/10.1007/s12517-017-3057-2.

USGS, 2019, https://earthquake.usgs.gov.

Worden, C. B., M. C. Gerstenberger, D. A. Rhoades, and D. J. Wald, 2012, Probabilistic relationships between ground-motion parameters and modified Mercalli intensity in California: Bulletin of the Seismological Society of America, **102**, no. 1, 204–221, https://doi.org/10.1785/0120110156.

Youd, T. L., 1977, Packing changes and liquefaction susceptibility: Journal of the Geotechnical Engineering Division, **103**, no. 8, 918–922, https://doi.org/10.1061/AJGEB6.0000478.

Youd, T. L., 1995, Liquefaction-induced lateral ground displacement: Presented at the Third International Conferences on Recent Advances in Geotechnical Earthquake Engineering and Soil Dynamics.

Redistribution subject to SEG license or copyright; see Terms of Use at http://library.seg.org/page/policies/terms
DOI:10.1190/tle40080590.1